Wavelet Spatio-Temporal Change Detection on Multitemporal SAR Images

Rodney V. Fonseca, Rogério G. Negri, Aluísio Pinheiro, and Abdourrahmane Mahamane Atto, *Senior Member, IEEE*

***Abstract*— In this article, we introduce the wavelet energies correlation screening (WECS), an unsupervised method to detect spatio-temporal changes on multitemporal SAR images. The procedure is based on wavelet approximation for the multitemporal images, wavelet energy apportionment, and ultrahigh-dimensional correlation screening for the wavelet coefficients. We show WECS's performance on simulated multitemporal image data. We also evaluate the proposed method on a time series of 85 Sentinel-1 images of a forest region at the border of Brazil and French Guiana. Comparisons with well-known change detection methods found in the literature highlight the proposal's superiority in terms of change detection accuracy. Additionally, the introduced method has simple architecture and low computational cost.**

***Index Terms*—Change detection, multitemporal images, remote sensing, simulated images, wavelets.**

I. Introduction

CHANGE detection in satellite images is an important issue pursued in remote sensing. It allows practitioners to identify and evaluate modifications on land surfaces. Its relevance may be exemplified by changes due to human activity, such as deforestation [1], rapid urbanization [2], and glacier melting [3].

Special attention has been given in the literature to change detection using synthetic aperture radar (SAR) images. Known to be unaffected by weather, cloud, and sunlight conditions, SAR images are an essential data source in change detection applications [4].

An issue with this type of data is that SAR's acquisition architecture brings a special kind of noise called speckle. This noise typically demands additional preprocessing of the images. Despeckling the SAR images has been the focus of research for a long time, and techniques are varied. For instance, Bhateja et al. [5] employ local statistics filters. Ma et al. [6] control speckle noise through likelihood-ratio tests. The authors in [7] and [8] reduce speckle in intensity SAR images via stochastic distances methods. The former does it with nonlocal means, while the latter employs Bernoulli sampling self-supervised deep learning ideas. Sebastianelli et al. [9] denoise Sentinel-1 SAR images through deep learning based on convolutional neural networks.

Speckle reduction has also been pursued using different wavelet proposals. Fukuda and Hirosawa [10] denoise SAR images by reducing the amplitude of detail wavelet coefficients while preserving edges. Dong et al. [11] reduce speckle noise by recursive wavelet transforms. Solbø and Eltoft [12] propose the wavelet version of the λ-MAP denoising filter in the so-called λ-WMAP. Vidal-Pantaleoni and Martí [13] provide several thresholding options in the wavelet analysis of SAR images and compares its performance for speckle treatment. Bovolo and Bruzzone [4] propose a multiscale decomposition of the log-ratio SAR image. Gupta and R. Gupta [14] employ wavelet representation to despeckle SAR images, coupled with wavelet-based detection of geographical features. Liu et al. [15] use wavelet transforms to estimate the noise variance, which is then employed for noise reduction via weighted nuclear norm minimization and Grey theory. Penna and Mascarenhas [16] reduce noise by nonlocal means algorithms in the Haar wavelet domain.

Change detection in multitemporal SAR images has been studied with diverse methods. For example, Johnson and Kasischke [17] employ change vector analysis (CVA), while Bujor et al. [18] apply log-cumulants to detect spatio-temporal discontinuities in multitemporal SAR images. Gamba et al. [19] combine feature- and pixel-based techniques. The approach proposed by Celik [20] is the PCA K-Means (PCAKM), where a clustering process segregates the divergences extracted via principal component analysis. Zhang et al. [21] employ a sparse feature clustering network to attain unsupervised SAR image change detection. Sentinel-1 data are studied by Mastro et al. [22] with random forests. Zhang et al. [23] use histogram fitting error minimization when there are few changed areas, while Zhang et al. [24] detect changes via adaptive contourlet fusion clustering. Iteratively reweighted MAD method (IRMAD) is the proposal of Nielsen [25]. Li et al. [26] use slow feature analysis and image fusion. Zhuang et al. [27] rely on the

Manuscript received 26 January 2023; revised 28 March 2023; accepted 17 April 2023. Date of publication 20 April 2023; date of current version 2 May 2023. This work was supported in part by FAPESP under Grant 2016/24469-6, Grant 2018/04654-9, 2021/01305-6, and Grant 2021/04513-9 and in part by CNPq under Grant 309230/2017-9 and Grant 310991/2020-0. The work of Rodney V. Fonseca was supported by the Morá Miriam Rozen Gerber Fellowship for Brazilian postdocs. *(Corresponding author: Rodney V. Fonseca.)*

Rodney V. Fonseca is with the Department of Computer Science and Applied Mathematics, Weizmann Institute of Science, Rehovot 7632706, Israel (e-mail: rodney.fonseca@weizmann.ac.il).

Rogério G. Negri is with the Department of Environmental Engineering, São Paulo State University, São José dos Campos 12247-004, Brazil (e-mail: rogerio.negri@unesp.br).

Aluísio Pinheiro is with the Department of Statistics, University of Campinas, Campinas 13083-859, Brazil (e-mail: pinheiro@unicamp.br).

Abdourrahmane Mahamane Atto is with the LISTIC - Polytech Annecy-Chambéry, Université de Savoie, 74944 Annecy le Vieux Cedex, France (e-mail: abdourrahmane.atto@univ-savoie.fr).

Digital Object Identifier 10.1109/JSTARS.2023.3268601

progressive nonlocal theory to detect changes. Several recent studies perform change detection via different deep learning ideas [28], [29], [30], [31], [32]. The authors in [33] and [34] employ approaches based on probabilistic distributions for error terms and change detection matrices. The authors in [35] and [36] propose change detection methods based on clustering. The authors in [37] and [38] discuss the varied nonlocal mean filters. Compressed projection and image fusion are employed by Hou et al. [39]. Invariant slow feature analysis (ISFA) is employed by Wu et al. [40]. Deep slow feature analysis for change detection is the subject of [41]. Chen et al. [42] propose a change detection method driven by adaptive parameter estimation.

Besides the methodological differences in the aforementioned works, emphasis may be put on the area of potential applications. Lin et al. [43] discuss the performance of different methodologies for landslide detection through multitemporal SAR images. The authors in [44] and [45] present results of unsupervised change detection for urban areas. Change detection in multitemporal hyperspectral images is discussed in [46], [47], and [48].

Change detection analysis is classified either as supervised (training data are used to set up the method) or unsupervised (fully data-driven techniques). We focus here on unsupervised approaches [49], [50], [51], [52], [53], [54]. Most of these methods have been developed for pairs of images. Consequently, changes can be detected only when they represent some modification between the initial and final time instants. This disregards potentially relevant changes, which occur in intermediary instants of time and are subsequently reversed. Moreover, simultaneous analysis of many pairs of images can, even for time series of medium length, pose serious statistical burdens such as low power and high false positive ratios [55], [56], [57].

Change detection using SAR images is challenging due to the high dimensionality of multitemporal datasets associated with the speckle noise. In this context, a wavelet transform is a convenient tool, given its robustness to noisy data and the efficient algorithms available to compute it.

Wavelet-based methods have many advantages for a plethora of statistical applications, thanks to wavelet capabilities in capturing multiscale/resolution information [57]. Their computational efficiency and sparseness are especially relevant for large images and other high-dimensional data [55]. On the other hand, there are methods that have been successfully applied in high-dimensional statistical models but are still novel ideas in the wavelet and change detection literature.

We may summarize the literature on multitemporal SAR image change detection as follows. There is no single method in the literature that simultaneously deals with a time series of images longer than two, is based on wavelet representation of SAR images, presents a straightforward answer to the spatiotemporal detection of changes in a single step, is unsupervised, and is scalable, i.e., may be used for very large images and/or very long time series.

Motivated by the aforementioned discussion, we propose the wavelet energies correlation screening (WECS), a novel unsupervised change detection method to analyze *full time-series of SAR images*. WECS is based on ultra-high-dimensional feature screening of wavelet coefficients [56]. We show that it is possible to simultaneously use all instants of time and all image locations with an unsupervised technique. WECS yields straightforward results and provides accurate change detection with low false positive and false negative rates.

The remainder of this article is organized as follows. Basic concepts and definitions are presented in Section II. Section III introduces the problem and the proposed method. We show WECS' performance on simulated multitemporal image data in Section IV-B. In Section IV-C, we apply WECS to a time series of 85 satellite images acquired over the border region of Brazil and French Guiana. Finally, Section V concludes this article.

II. Background

Wavelet methods have been widely employed in the signal processing literature, especially for denoising and compression tasks [57]. Wavelets provide multiresolution decompositions, whereby a signal is represented by two types of values: approximation coefficients, which describe the average (coarse) behavior of the signal, and detail coefficients, which correspond to local (fine) characteristics. These coefficients are generally computed via a discrete wavelet transform. When the signal is a matrix, such a transform consists in applying low- and high-pass convolution filters to its rows and columns [55].

We apply wavelet transform to reduce speckle noise. Each image is represented by a matrix, and a low-pass filter is applied J times to rows and columns of the corresponding matrix. The value J is also called resolution level, a tuning parameter for wavelet smoothing. We use a discrete stationary wavelet transform, also known as nondecimated or redundant wavelets [58]. We do not apply here any specialized wavelet method to reduce speckle. Notwithstanding this, the attained performance does not show speckle's deleterious effects. The wavelet-denoised data are a time series of smoothed images.

Although the wavelet smoothing on images embraces an initial step to analyze the data, our main goal is to find the spatial changes over time. The smoothed images still contain many coefficients that need to be evaluated simultaneously, which characterizes a high-dimensional problem with multiple time series corresponding to each location in space. Consequently, retaining only the most essential locations driving overall modifications across time is desirable. Because our objective is twofold, i.e., detecting the times when changes occur, as well as the spatial locations where such changes take place, we employ *feature screening*, a method originally proposed for variable selection in high-dimensional regression models. The feature screening technique is a particularly efficient method to identify relevant variables, especially when the number of candidates is large [59].

With no loss of generality, we discuss the feature screening process under the linear regression model paradigm. Consider $\mathbf{y} = \sum_{i=1}^{p} \beta_i \mathbf{W}_i + \boldsymbol{\epsilon}$, where $\mathbf{y} \in \mathbb{R}^n$ is the response variable, $\mathbf{W}_1, \ldots, \mathbf{W}_p \in \mathbb{R}^n$ are p explanatory variables and $\boldsymbol{\epsilon} \in \mathbb{R}^n$ is a zero mean random error, and the parameters $\beta_1, \ldots, \beta_p \in \mathbb{R}$ are unknown. One is often interested in identifying which parameters are not zero, and consequently, determining which covariates $\mathbf{W}_i$ are essential to the model. An issue is that the dimension p is often much larger than the sample size n, but

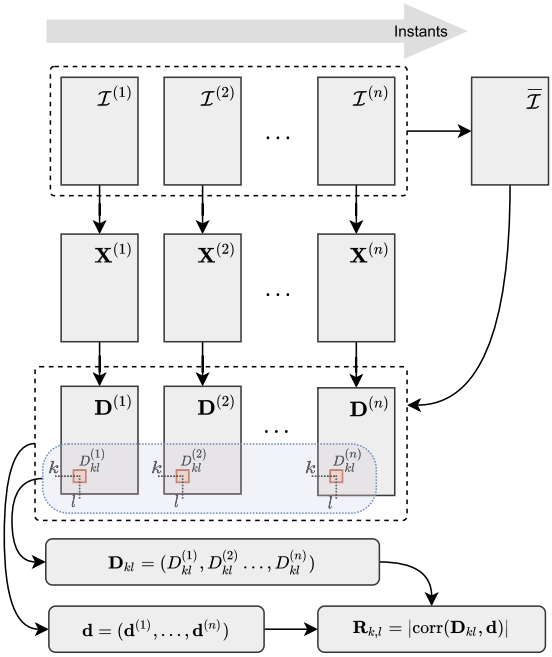

Fig. 1. Diagram of steps performed to apply WECS. $\mathcal{I}^{(j)}$ and $\mathbf{X}^{(j)}$ represent the raw and wavelet-smoothed jth image, respectively. $\mathbf{d}$ is the vector of overall changes. $\mathbf{D}^{(j)}$ is the matrix formed by the local measures of changes, $D_{kl}^{(j)}$ for the jth time instant.

only a handful of the β_i is different from zero. Feature screening consists in computing all sample correlations $\mathrm{corr}(\mathbf{y}, \mathbf{W}_i)$ between response and explanatory variables, and then, selecting those covariates whose correlations are among the highest in absolute value. Under suitable conditions, this method selects with very high probability a set of indices containing all i such that $\beta_i \neq 0$. We show that a similar idea can be used to detect change locations in multitemporal images.

III. Wavelet Energy Correlation Screening

Our analysis is performed on the wavelet coefficients computed for the multitemporal images. We use these coefficients to calculate change measures for each pixel individually and for the whole image. We classify as change locations the pixels whose measures are highly correlated with the values computed for the whole picture. Fig. 1 depicts a high-level description of the proposed method.

Let $\mathcal{I}^{(1)}, \ldots, \mathcal{I}^{(n)} \in \mathbb{R}^{u \times v}$ be a time series of images (matrices) defined on support $\mathcal{S} = \{1, \ldots, u\} \times \{1, \ldots, v\} \subset \mathbb{N}^2$. The matrix $\mathcal{I}^{(m)}$ represents a region of $u \times v$ locations at an instant $m \in \{1, \ldots, n\}$. We have the following two goals:

1) finding instants m when relevant changes happen;
2) finding which regions $(k, l) \in \mathcal{S}$ are associated with the observed changes over time.

We aim to attain both goals simultaneously. We apply the bidimensional stationary discrete wavelet transform on each matrix $\mathcal{I}^{(m)}$, resulting in a matrix of approximation wavelet coefficients, say $\mathbf{X}^{(m)}$. We interpret $\mathbf{X}^{(m)}$ as a denoised version of $\mathcal{I}^{(m)}$, defined on the same support $\mathcal{S}$. The level of denoising is controlled by the resolution level J, which must satisfy $J \in \{1, 2, \ldots, \lfloor \log_2(\min\{u, v\}) \rfloor\}$. The higher J is, the smoother the image represented by $\mathbf{X}^{(m)}$.

We can then consider further apportioning the total $\mathbb{L}_2$ energy of the series $\{\mathbf{X}^{(m)}\}_{m=1}^n$ as

$$\sum_{m=1}^{n} \|\mathbf{X}^{(m)}\|_F^2 = n\|\overline{\mathcal{I}}\|_F^2 + 2n\langle \overline{\mathbf{X}} - \overline{\mathcal{I}}, \overline{\mathcal{I}} \rangle_F + \sum_{m=1}^{n} \|\mathbf{X}^{(m)} - \overline{\mathcal{I}}\|_F^2 \quad (1)$$

where $\overline{\mathcal{I}} = \frac{1}{n}\sum_{m=1}^n \mathcal{I}^{(m)}$ and $\overline{\mathbf{X}} = \frac{1}{n}\sum_{m=1}^n \mathbf{X}^{(m)}$ are the average image and smoothed image, respectively, and $\|\cdot\|_F$ and $\langle \cdot, \cdot \rangle_F$ represent the Frobenius norm and inner product, respectively.

The last term on the right-hand side of (1) measures the deviations between the denoised image $\mathbf{X}^{(m)}$ and the *average image* $\overline{\mathcal{I}}$ at distinct instants. We use the deviations $\{\|\mathbf{X}^{(m)} - \overline{\mathcal{I}}\|_F^2\}_{m=1}^n$ as proxies to relevant changes over time.

Let $X_{kl}^{(m)}$ and $\overline{\mathcal{I}}_{kl}$ be the entry (k, l) of $\mathbf{X}^{(m)}$ and $\overline{\mathcal{I}}$, respectively. We define the squared mean deviations by

$$D_{kl}^{(m)} = \left(\mathbf{X}_{kl}^{(m)} - \overline{\mathcal{I}}_{kl}\right)^2. \quad (2)$$

The overall deviation at instant m is measured by

$$\mathbf{d}^{(m)} = \sum_{k=1}^{u}\sum_{l=1}^{v} D_{kl}^{(m)}. \quad (3)$$

The value $\mathbf{d}^{(m)}$ is simply $\|\mathbf{X}^{(m)} - \overline{\mathcal{I}}\|_F^2$, which quantifies the overall change in the image. A large value of $\mathbf{d}^{(m)}$ indicates that a relevant change happens at instant m. Hence, we may associate changes with the temporal dynamics on $\{\mathbf{d}^{(m)}\}_{m=1}^n$.

The spatio-temporal character of our proposal may be understood as follows. Changes in space are associated with the temporal dynamics of the matrices $D_{kl}^{(m)}$, defined in (2). Each $D_{kl}^{(m)}$ measures the change at location (k, l) and instant m. Let $\mathbf{D}_{kl} = (D_{kl}^{(1)}, \ldots, D_{kl}^{(n)})$ be the sequence of n squared deviations at location (k, l) and let $\mathbf{d} = (\mathbf{d}^{(1)}, \ldots, \mathbf{d}^{(n)})$. Whenever $\mathbf{D}_{kl}$ behaves similarly to $\mathbf{d}$, we have an indication that location (k, l) contributes to the overall change. We quantify this association with the absolute value of the Pearson correlation between the two sequences

$$R_{kl} = |\mathrm{corr}\,(\mathbf{D}_{kl}, \mathbf{d})\,|. \quad (4)$$

Feature screening by Pearson correlation in high-dimensional regression models is an efficient selection criterion [59]. In our case, these correlations automatically identify the locations where important changes are observed in the multitemporal images. Hence, if R_{kl} has a large value, the location (k, l) can be seen as a change point. Such an association measure is based on the *linear relation* between the squared mean deviations computed for individual locations and the whole image. We denote the matrix of absolute correlations as $\mathbf{R} = \{R_{kl}\}$.

Define $\mathcal{M}^\star \subseteq \mathcal{S}$ as the indicator mapping of *relevant* indices for changes over the image series with respect to $\overline{\mathcal{I}}$. The entries

of $\mathcal{M}^\star$ indicate where *changes in* $\{\mathcal{I}^{(m)}\}_{m=1}^n$ *with respect to* $\overline{\mathcal{I}}$ *are affected by local changes in the images*.

If we apply the index dichotomy defined by $\mathcal{M}^\star$ to (3), we have

$$\mathbf{d}^{(m)} = \sum_{(k,l)\in\mathcal{S}} \beta_{kl} D_{kl}^{(m)} + \varepsilon^{(m)} \tag{5}$$

where β_{kl} are non-null regression coefficients for $(k,l) \in \mathcal{M}^\star$, and $\varepsilon^{(m)}$ are stochastic error terms. The error terms allow for both the apportionment of spurious correlation for indices not in $\mathcal{M}^\star$ as well as for the energies not represented by the wavelet smoothing.

It is a well-known property of discrete wavelet transforms that it statistically decorrelates the original data [55], [57]. For instance, this motivates the use of WECS instead of a nonwavelet version of energy correlation, since wavelets will result in sparser representations for $\mathcal{M}^\star$. Moreover, the sure screening theoretical results for independent data motivates our conjecture that the regression setup given by (5) should have a good performance. A rigorous proof for dependent data such as ours is beyond the scope of this manuscript, but the numerical results provide us with solid evidence.

Finally, an empirical mapping of change locations may be stated as

$$\mathcal{M}_\tau = \{(k,l) \in \mathcal{S} : |R_{kl}| > \tau\} \tag{6}$$

where $\tau > 0$ is some convenient threshold value. For suitable values of τ, the empirical set $\mathcal{M}_\tau$ has high probability of detecting the correct change locations in $\mathcal{M}^\star$ [56], [59].

IV. Experiments

A. Experimental Design

We present two studies to evaluate the proposed method's performance in detecting changes in simulated and real data. We compare WECS with other methods. The first method is a simple thresholding of aggregate absolute difference images, which we call TAAD. The second method follows the diagram in Fig. 1, but we use directly the images $\mathcal{I}^{(m)}$ to compute the matrices of squared differences $\mathbf{D}^{(m)}$, skipping the wavelet-smoothing step. Since this method also involves energy correlation screening, we call it ECS. The other methods are change vector analysis (CVA) [17], the PCA K-Means (PCAKM) [20], iteratively reweighted MAD (IRMAD) [25], the invariant slow feature analysis (ISFA) [40], and change detection with a fusion of multiple wavelet kernels (FMW) [60]. Besides FMW, other wavelet approaches were implemented [61], [62] but did not provide good results, hence they are not shown here.

The application of difference images has a long tradition in the literature of change detection in remote sensing [49]. This motivates us to compute the difference between each pair of consecutive images in the time series. To apply TAAD, we first compute $A_{kl} = \sum_{m=2}^n |\mathcal{I}_{kl}^{(m)} - \mathcal{I}_{kl}^{(m-1)}|$ for each location (k,l). Then, we form a matrix $\mathbf{A}$ whose entries are values A_{kl} are divided by $\max_{k,l} |A_{kl}|$, which results in a number in the interval [0,1]. A large value in $\mathbf{A}$ is an indication that a change happened at the corresponding location. The final step of TAAD applies thresholding on all elements of $\mathbf{A}$.

The method ECS is analogous to WECS, in the sense that the image's energy is also apportioned. While WECS does it for the wavelet-transformed images, ECS uses $\mathcal{I}^{(m)}$ instead of the wavelet coefficients $\mathbf{X}^{(m)}$. Hence, the squared differences in (3) are computed as $(\mathcal{I}_{kl}^{(m)} - \overline{\mathcal{I}}_{kl})^2$. The resulting Pearson correlation matrix from ECS shall be denoted as $\widetilde{\mathbf{R}}$.

The other approaches (CVA, PCAKM, IRMAD, ISFA, FMW) are bitemporal methods. They can only be applied for two previously selected instants of the adopted image time series. In our analysis, we apply these methods only to the first and last images of the series.

In Section IV-B, we analyze simulated multitemporal images, for which we know where and when changes happen. We use the simulated data to identify the most appropriate wavelet family and resolution level J. We analyze the following wavelets: Haar (haar), Daubechies of orders 2 and 4 (db2, db4), Coiflets of order 4 (coif4), and Symlets of orders 2 and 4 (sym2, sym4) [63], [64]. For methods that provide a range of values in [0,1], like WECS, ECS, and TAAD, we can compute receiver operating characteristic (ROC) curves. For the bitemporal methods, we only have change and nonchange regions (0's or 1's). Thus, only change maps are provided for the results of such methods.

Section IV-C presents a real-world application of SAR image series. Change detection accuracy is measured with the following criteria: F1-Score [65], True/False Positive/Negative (TP, TN, FP, and FN) rates, the kappa coefficient, and the variance of kappa [66]. Additionally, computational run times are presented and discussed.

We used a computer with an Intel Intel i-7 processor ($8\,\text{core}$, $3.5\,\text{GHz}$), and $16\,\text{GB}$ of RAM running the Ubuntu Linux version 20.04 operating system. The code of the proposed method is freely available at https://github.com/rodneyfv/wecs.

B. Simulated Data Analysis

We consider here a sequence of four different images, each one having two bands consisting of the same figure. The figures have different types of ellipses in a blank space. This sequence is repeated 20 times to form a series of 80 multitemporal images. Each noiseless image is represented by two matrices, one for each band. These matrices have binary entries, with ones denoting where the ellipses occur and zeroes elsewhere. The ellipses are the changes in the images. To form an observed image $\mathcal{I}^{(m)}$, we add independent noise following a Gamma distribution to each entry in the noiseless matrices. For band 1, change and nonchange regions receive noise following $\text{Gamma}(119.95, 0.25)$ and $\text{Gamma}(38, 0.8)$, respectively, where $\text{Gamma}(a, b)$ is a Gamma distribution with shape and scale parameters a and b, respectively. For band 2, we add noise following $\text{Gamma}(99.2, 0.35)$ and $\text{Gamma}(43.63, 0.81)$ to change and nonchange regions, respectively. These values were estimated from the dataset presented in Section IV-C. We also applied a mean filter with a 3×3 window running on the matrices of each band, to simulate spatial dependence.

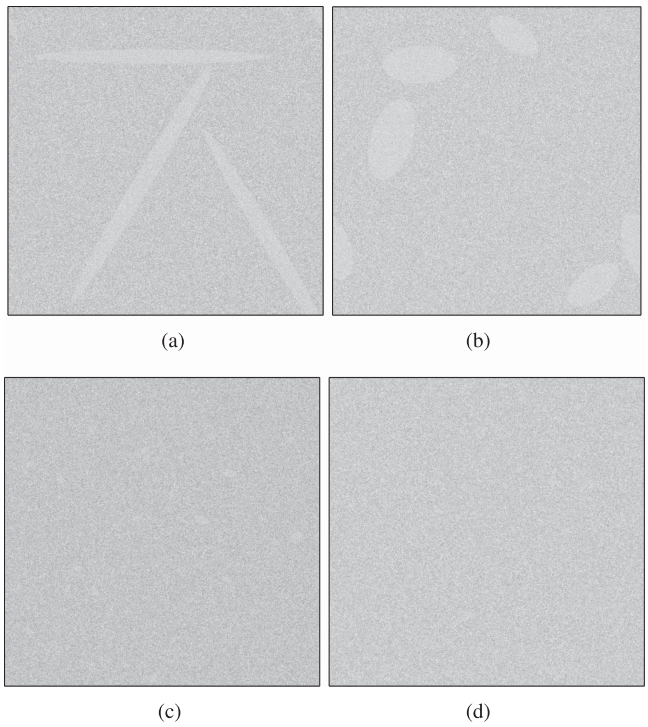

Fig. 2. Amplitude of the first four simulated multitemporal images. Changes appear as white ellipses. (a) $\mathcal{I}^{(1)}$. (b) $\mathcal{I}^{(2)}$. (c) $\mathcal{I}^{(3)}$. (d) $\mathcal{I}^{(4)}$.

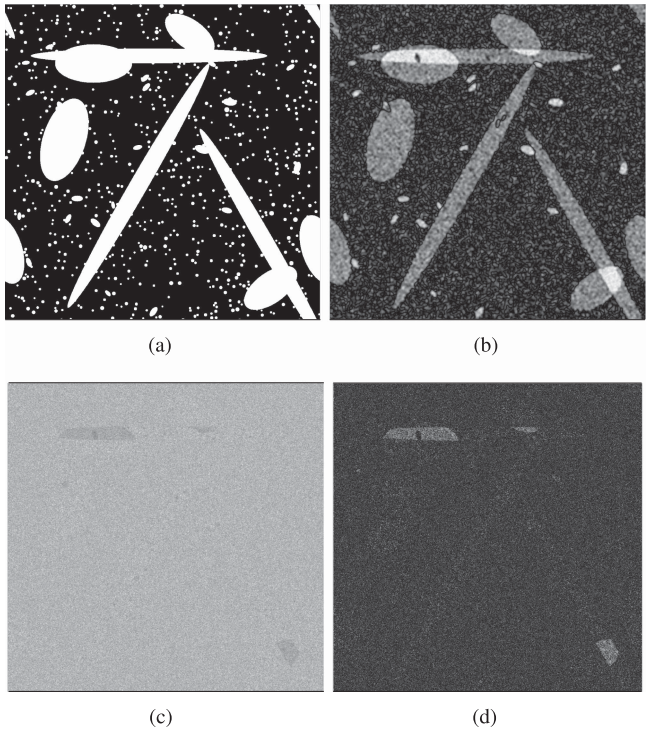

Fig. 3. (a) Change/nonchange regions in simulated data and (b)–(d) results provided by WECS, TAAD, and ECS before a thresholding process. (a) Total changes. (b) WECS (db2, $J = 3$) – $\mathbf{R}$. (c) TAAD – $\mathbf{A}$. (d) ECS – $\widetilde{\mathbf{R}}$.

WECS is applied to the amplitudes of the pixel values of the simulated images, that is, the Euclidean norm of pixel values in different bands. Examples of the amplitudes of the first four instants are shown in Fig. 2. The first image $\mathcal{I}^{(1)}$ contains three elongated ellipses. The second image $\mathcal{I}^{(2)}$ has shorter but wider ellipses. The other instants $\mathcal{I}^{(3)}$ and $\mathcal{I}^{(4)}$ display smaller changes, practically unnoticeable due to noise. Fig. 3(a) shows all true change locations, where white regions (i.e., "ones") indicate where change happens at least once in the series.

Applying WECS to these images, we obtain a matrix $\mathbf{R}$ of correlations computed through (4). Fig. 3(b) presents the $\mathbf{R}$ computed for the simulated images. Similarly, Fig. 3(c) and (d) depicts the matrices $\mathbf{A}$ and $\widetilde{\mathbf{R}}$ provided by TAAD and ECS, respectively. We visually infer from Fig. 3 that WECS outperforms both ECS and TAAD.

Fig. 4(a) presents the ROC curves for WECS with different wavelet bases. All instances adopt the resolution $J = 3$. We conclude that db2 and sym2 deliver the best tradeoff between true and false positive ratios, i.e., high true positive ratios even when the false positive ratios are low. Thus, we shall use the db2 wavelet basis in the remaining experiments and analyses.

Fig. 4(b) depicts the ROC curves for resolution levels $J \in \{1, \ldots, 5\}$. These curves provide evidence that J equal to 3 or 4 leads to the best performances when the images are very noisy. $J = 3$ has a slight advantage since it demands fewer decomposition levels.

The ROC curves in Fig. 5(a) present the performances of WECS, TAAD, and ECS. WECS clearly has superior performance. ECS's low performance shows that it is not advisable to simply swap the wavelet transform by a "deviation image" into the proposed correlation screening pipeline. This result for ECS

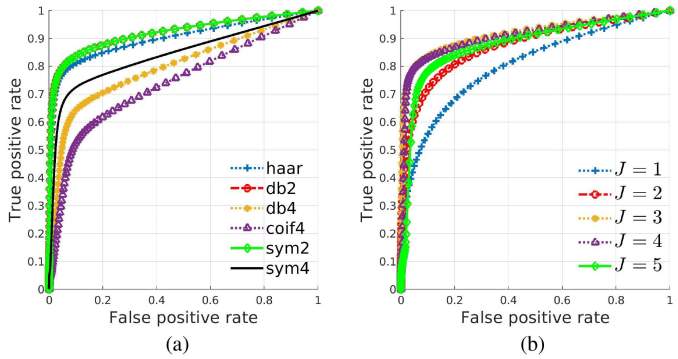

Fig. 4. ROC curves related to the experiment with simulated dataset. (a) WECS with $J = 3$. (b) WECS with db2 basis.

reinforces the importance of wavelet smoothing in the context of the proposed method. Since the noise level is high, we can also see that TAAD has a very poor performance. For the bitemporal methods, we only have change maps and are not able to compute ROC curves. Fig. 5(b)–(f) displays the output of the bitemporal methods applied on the first and last images of the simulated series. Compared to WECS' results in Fig. 3(a), the outputs of the bitemporal methods are worse, highlighting the importance of analyzing the whole time series of images.

We also present a simulation to evaluate how WECS performs in detecting small changes [23]. Analogously to the previous simulation study, we consider a sequence of four images. This time, only one image containing small ellipses is used to represent changes. The first noiseless image is illustrated in Fig. 6(a). The other three noiseless images in the series are

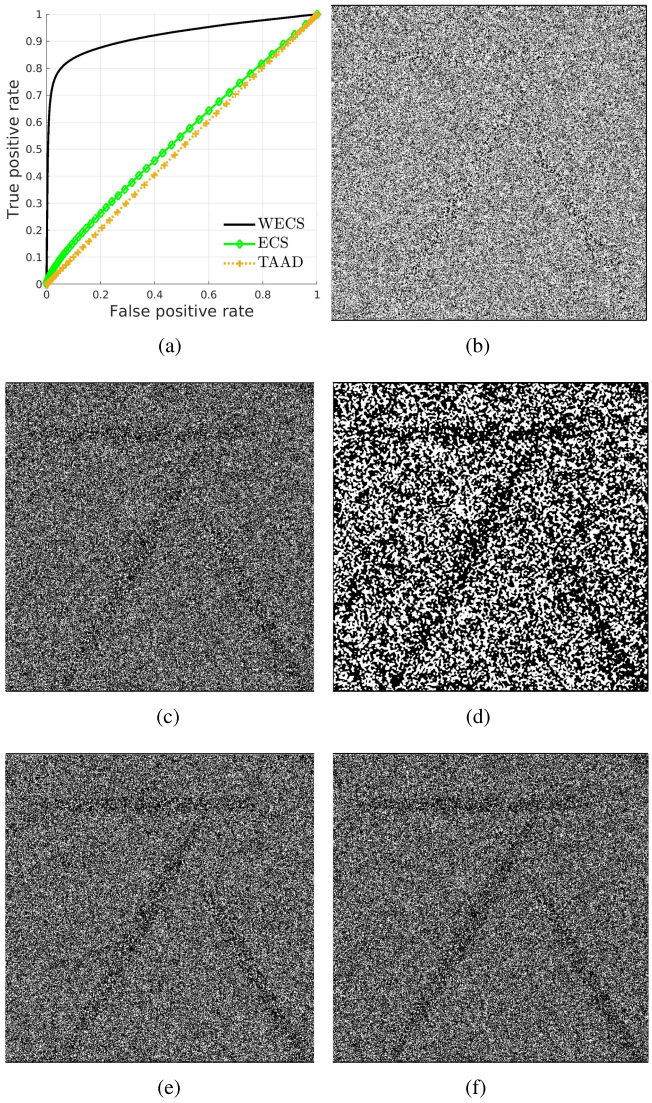

Fig. 5. ROC curves for WECS, TAAD, and ECS. Other plots are change maps of bitemporal methods applied to the first and last simulated images. (a) ROC curve. (b) FMW. (c) CVA. (d) PCAKM. (e) MAD. (f) ISFA.

made of matrices filled with zeroes. This sequence is repeated 20 times to form a sequence of 80 images. The observed images are generated by adding independent Gamma noise in the same way as the previous simulation. Fig. 6(b) shows the amplitude of the first noisy image corresponding to an instant with changes, which are practically unnoticeable to the naked eye. Fig. 6(c) shows the matrix **R** of correlations computed with WECS and Fig. 6(d) shows the ROC curves for WECS, TAAD, and ECS.

Once again, we notice that WECS provides the best results. Moreover, we note that WECS performs equally well in the small area's problem as it does in the general case, with no need for any modifications in the algorithm. We should emphasize here that the choice of $J = 3$ is more convenient than $J = 4$ to detect changes in noisy images. If the noise level were not so high, a lower J could provide better results.

C. Actual Remote Sensing Application

In this section, we compare the performance of WECS, TAAD, ECS, CVA, PCAKM, IRMAD, and ISFA in a real-world

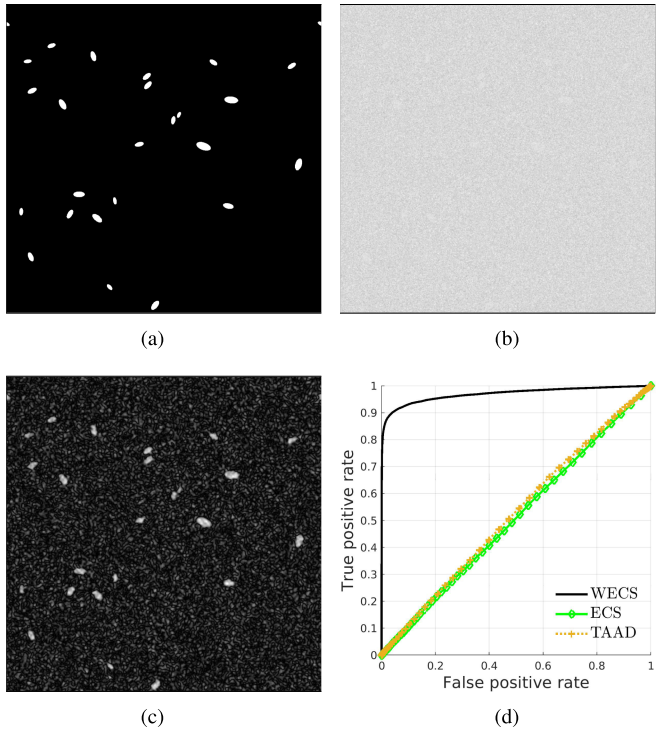

Fig. 6. Experiment of small change detection. (a) Changes locations. (b) Noisy image with changes. (c) WECS – **R**. (d) ROC curve.

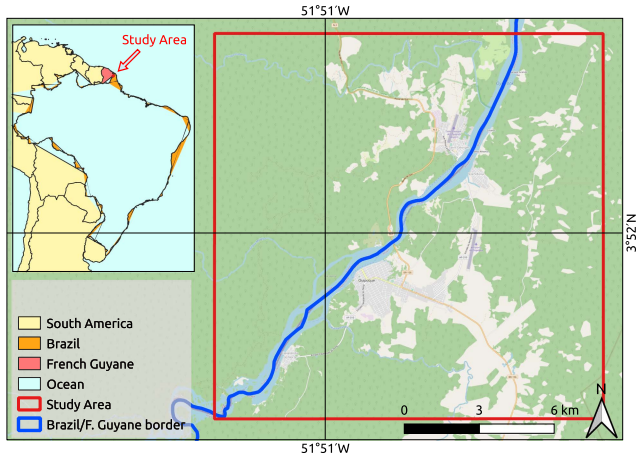

Fig. 7. Study area location.

application. Since FMW did not perform so well in the simulations, as we can see in Fig. 5(b), we decided not to apply this method. We employ for WECS the db2 wavelet basis and resolution level $J = 2$. We tried other values of J, but $J = 2$ provides better results.

Our data consist of 85 multitemporal images of a forest region at the border of Brazil and the French Guiana, as shown in Fig. 7. The images' time instants vary from December 26th, 2015 to December 3rd, 2017. They were obtained from the *Sentinel-1 SAR GRD* dataset, maintained by the European Space Agency [67].

Each image contains the amplitude signal backscatters relative to VV and VH polarizations, a spatial resolution of 10 m,

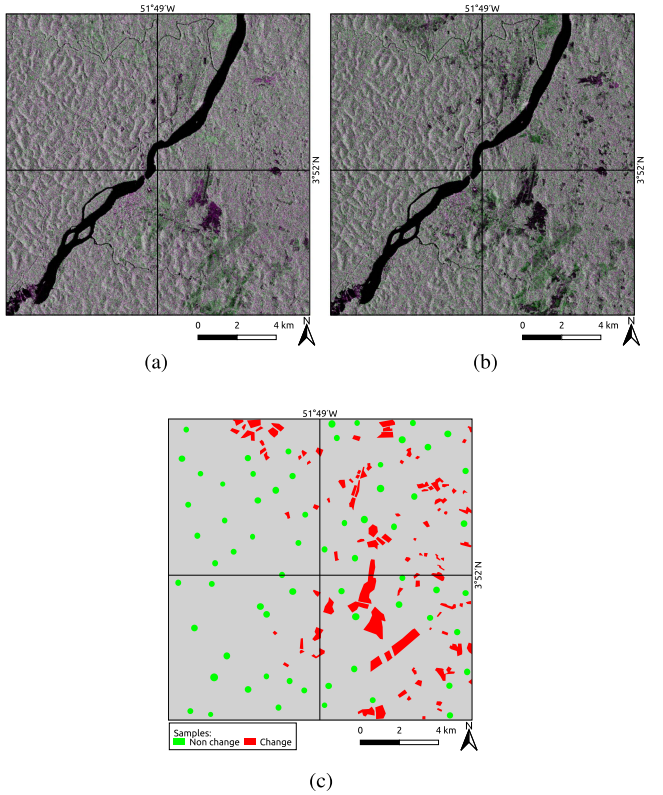

Fig. 8. (a) and (b) First and last images in the adopted multitemporal image series, in VV-HV-VV RGB color composition, and (c) reference samples. (a) December 26th 2015. (b) December 3rd 2017. (c) Reference change and nonchange samples.

and support of 1538×1556 pixels wide in ground range projection. Fig. 8(a) and 8(b) depicts the first and last images of the time series, where it is possible to compare and identify some landscape changes.

After careful visual inspection of the backscatter profile of each image in the series, it is possible to identify the regions where land-cover changes or does not change. This allows us to collect reference samples regarding the "change" and "nonchange" conditions. Such samples are needed to compute the accuracy measures mentioned in Section IV-A. These reference samples are presented in Fig. 8(c).

We should recall that WECS is applied to matrices corresponding to the observed images. Hence, the dual-polarized images are combined into a single-band representation considering the so-called "span" image $\mathcal{I}_{kl}^{(m)} = \sqrt{(\mathrm{VV}_{kl}^{(m)})^2 + (\mathrm{VH}_{kl}^{(m)})^2}$, with VV and VH representing the available polarizations.

Fig. 9 presents the overall deviations $\mathbf{d}^{(m)}$ for $m = 1, \ldots, 85$, computed as described in (3). The deviations $\mathbf{d}^{(m)}$ vary around the value 9.5. When $\mathbf{d}^{(m)}$ is much larger than 9.5 (like $m = 30$), we may have an instant where relevant changes occur. When $\mathbf{d}^{(m)}$ is much lower than 9.5 (like $m = 1$ and $m = 59$), the corresponding image is similar to the average image, i.e., m is not an instant where many changes happen. For instance, the wavelet representation at each mentioned instant (i.e., $\mathbf{X}^{(1)}$, $\mathbf{X}^{(30)}$, and $\mathbf{X}^{(59)}$) and the mean image $\overline{\mathcal{I}}$ are exhibited in Fig. 10. While $\mathbf{X}^{(1)}$ shares similarities with $\overline{\mathcal{I}}$, evident changes increase in $\mathbf{X}^{(30)}$.

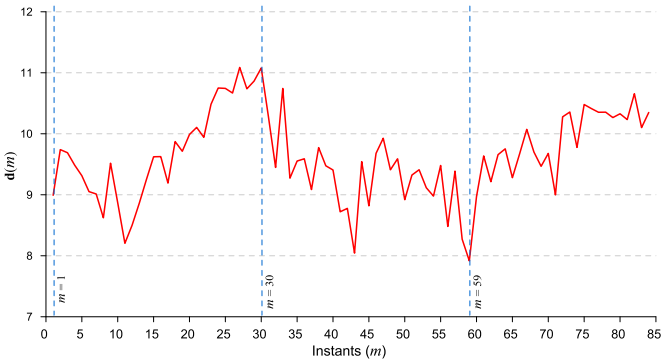

Fig. 9. Plot of $\mathbf{d}^{(m)}$ for $m = 1, \ldots, 85$. Distinct deviations occur at $m = 1$ (intermediate), 30 (high), and 59 (low).

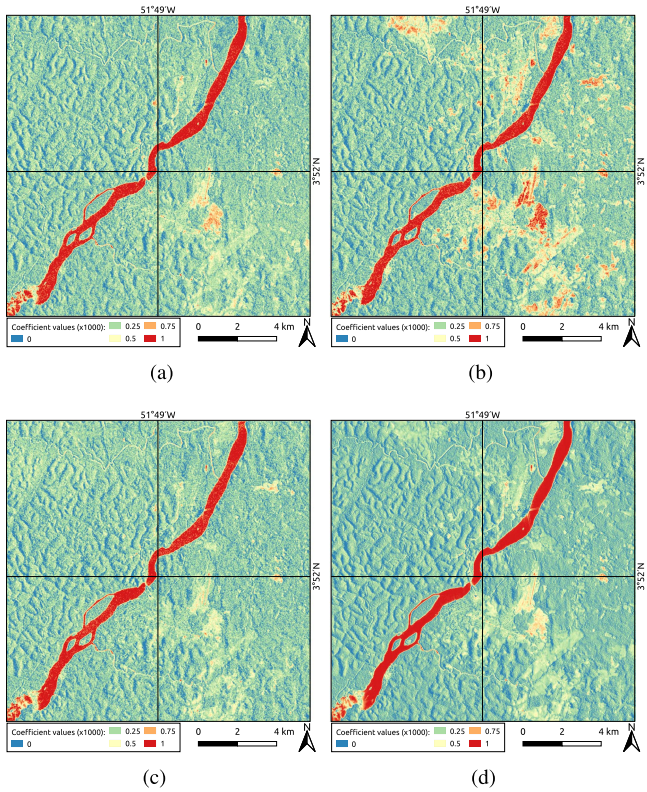

Fig. 10. Images $\mathbf{X}^{(m)}$ for $m = 1, 30, 59$ and mean image $\overline{\mathcal{I}}$. (a) $m = 1$. (b) $m = 30$. (c) $m = 59$. (d) $\overline{\mathcal{I}}$.

Reversely, $\mathbf{X}^{(59)}$ offers a low contribution for identifying change regions.

Fig. 11 depicts $\mathbf{R}$, where high values stand for regions with changes in their land cover over time as detected by WECS. The methods ECS, TAAD, CVA, PCAKM, IRMAD, and ISFA also output matrices of change measures for all locations. Thresholding the matrices' values is a convenient way of determining a binary map $\mathcal{M}_\tau$ of "change" and "nonchange" areas. Two choices of cut-off value τ are employed. Otsu (OT) [68] and Kittler–Illingworth (KI) [69] thresholding techniques have been successfully employed for change detection purposes [17], [25], [40], [53]. Both OT and KI thresholding are applied to WECS, ECS, and TAAD, while CVA and ISFA are thresholded via

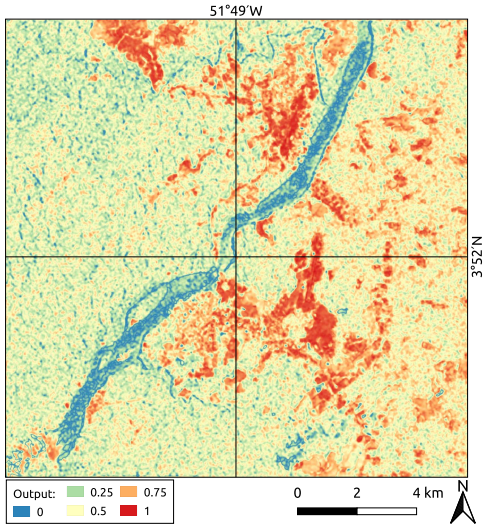

WECS – **R**

Fig. 11. WECS "tendency of change" matrix **R**, computed as described in (4).

TABLE I
ACCURACY VALUES SUMMARY AND COMPUTATIONAL RUN TIMES

Method	WECS		ECS		TAAD	
Threshold	OT	KI	OT	KI	OT	KI
F1-Score	**0.940**	0.843	0.802	0.774	0.639	0.617
Kappa	**0.818**	0.637	0.545	0.513	0.271	0.256
Var. of kappa	6.90	2.65	1.97	1.71	0.83	0.76
Time (s)	104.68		51.1		7.12	

Method	CVA	PCAKM	IRMAD	ISFA
F1-Score	0.624	0.624	0.579	0.519
Kappa	0.176	0.277	0.106	0.070
Var. of kappa	0.73	0.79	0.60	0.49
Time (s)	6.61	57.70	**6.13**	18.64

The variance of Kappa is multiplied by $\times 10_5$.

OT. PCAKM and IRMAD are computed with different approaches [20], [25].

The accuracy of the computed binary maps $\mathcal{M}_\tau$ is measured in terms of the F1-Score and kappa coefficient based on the reference ground-truth samples [see Fig. 8(c)]. Table I presents the accuracy measures computed for all the analyzed methods.

Notice that WECS with the OT algorithm presents the best performance of detecting change locations without increasing/inflating the number of false positives (FP). This can be seen from the higher F1-Score level. Moreover, according to the kappa coefficient, WECS also delivers a more balanced correct classification regarding the change and nonchange areas. Furthermore, based on the kappa values and respective variances, the difference between any pair of results is significant at 1%.

WECS-KI performance is surpassed by WECS-OT. Notwithstanding the importance of the thresholding algorithm, we should emphasize that both WECS-based methods provide more accurate results than all other methods considered.

Fig. 12 depicts the most accurate change/nonchange maps according to the measures in Table I. It is possible to verify that while TAAD-KI and PCAKM assign the water body as a "change region," they do not detect other change locations, like the northwest and southeast portions in the second and fourth quadrants. Regarding CVA, IRMAD, and ISFA, their results have a noise-corrupt character, with many false positive points.

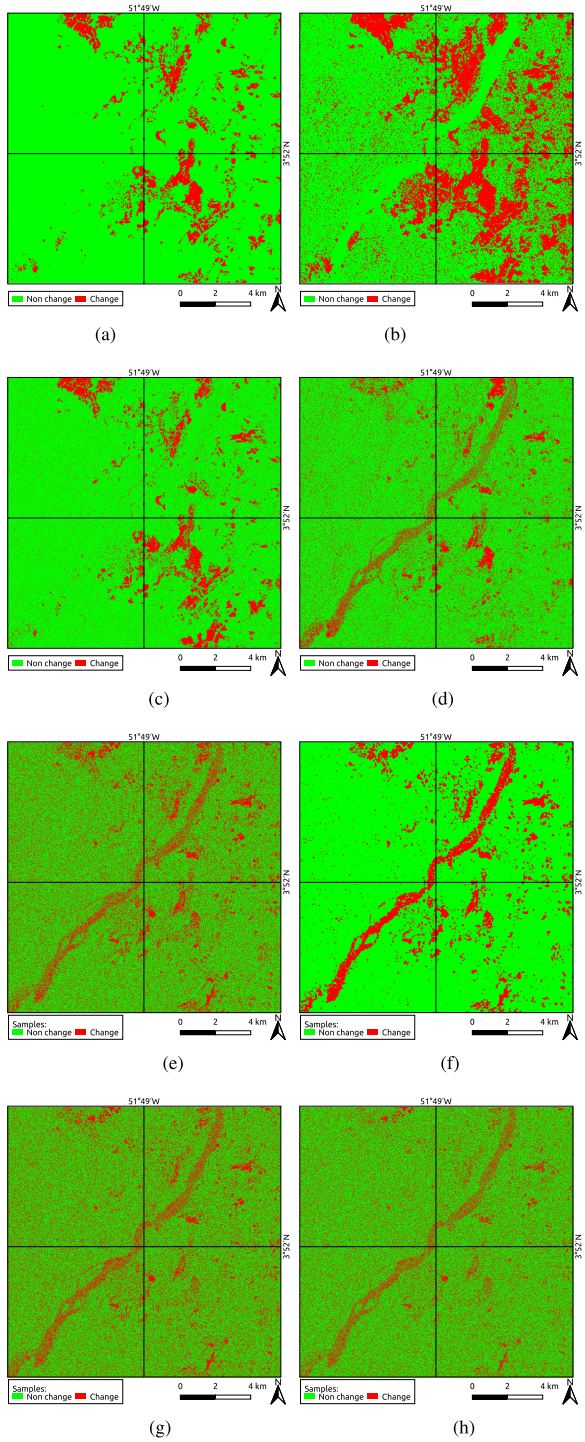

Fig. 12. Resulting change maps from the analyzed methods. (a) WECS-KI. (b) WECS-OT. (c) ECS-OT. (d) TAAD-OT. (e) CVA. (f) PCAKM. (g) IRMAD. (h) ISFA.

As previously observed, WECS equipped with the KI algorithm provides a homogeneous mapping over the nonchange areas [west portion—second and third quadrants of Fig. 12(a)], accurate detection over the change regions, and low inclusion (FP) and exclusion (FN) error rates. In adopting the OT

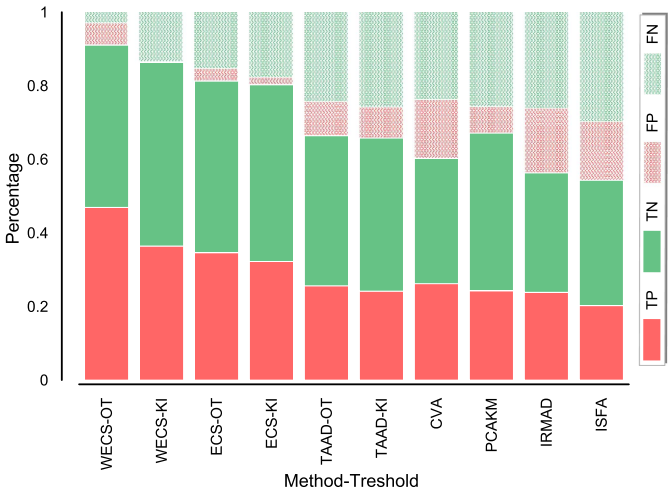

Fig. 13. Solid bars correspond to percentages of true positives and true negatives, whereas blurred bars correspond to false positives and false negatives. The red and green bars represent the percentage of change and nonchange regions detected, respectively.

algorithm, the inclusion error increases, resulting in a less-regularized change/nonchange map.

The proportions of True/False Positive/Negative assigned to the analyzed methods are summarized in Fig. 13 and corroborate the aforementioned discussion.

The computational run times are given in Table I. Recall that CVA, PCAKM, IRMAD, and ISFA are applied only on the first and last images of the time series, whereas WECS, TAAD, and ECS use all 85 images. A fair comparison would require the times for CVA, PCAKM, IRMAD, and ISFA to be multiplied by $85 \times 42 = 3570$. WECS's run time is not excessive in the context of remote sensing image processing. Moreover, WECS systematically provides more accurate results.

D. Discussion

Change detection in multitemporal satellite images can be characterized as a high-dimensional problem because a large number of pixels must be analyzed simultaneously. Therefore, methods for such analysis should be not only accurate but also simple enough to be applicable when the data are large. Pearson correlation and wavelet transforms are well-known methods in science and engineering. Still, their combination has not been explored for application in change detection on time series of satellite images. WECS is an approach that benefits from the straightforwardness of these measures, and it is shown to provide accurate results in empirical studies. Desirable properties in high-dimensional data analysis such as scalability, interpretability, robustness, and flexibility may be all associated to WECS.

The change measures computed via WECS are correlations between pixel-level and whole image values. Therefore, WECS is not tailored for bitemporal images. A high correlation in WECS means that the pixel-level dynamic behavior strongly resembles the overall dynamic behavior of the time series. For instance, suppose a series of images in which changes do exist over time. These changes may be meaningful or simple random fluctuations due to speckle. Either way, a high correlation in WECS is interpreted as the pixel behaving over time as the overall dynamic behavior. Before applying WECS, the overall change measure must be analyzed to assess whether and how the whole image changes with time. Such a dynamic behavior is observed, for example, in Fig. 9 for the forest data.

WECS is based on the idea of feature correlation screening [59]. Given the theoretical results available for this screening technique in regression models and the empirical results in Section IV, it is reasonable to postulate that WECS would have good theoretical results on the proposed application as well. However, the challenges would be to account for both the spatial and temporal dependence and their interconnections. Finally, the application of WECS' idea for satellite images other than SAR should take different aspects into consideration, like the type of noise, the number of channels, the sampling frequency of the images, etc. These aforementioned aspects demand further research.

The comparisons with other change detection methods using remote sensing data demonstrate the proposal's superiority in terms of F1-Score and kappa coefficient (see Table I). The resulting change maps (see Fig. 12) support the quantitative results, where it is possible to verify a more consistent distinction between change and nonchange areas, for example, by fairly not identifying the river crossing the study area [see Figs. 7 and 8(c)] as a "change" region.

V. Conclusion

We present WECS, a novel way of detecting changes in multitemporal satellite images. WECS uses the information of the whole time series of images and is based on wavelet representation of SAR images. It presents a straightforward answer to the spatio-temporal detection of changes in a single step, and is unsupervised and is scalable, i.e., may be used for very large images and/or very long time series. It uses correlation screening for ultrahigh dimensional data to identify which locations (pixels) are the most related to an overall change measure of the image time series. Thereupon, WECS is expected to provide a set of change points in space, such that this set contains all real changes with high probability.

The performance of WECS is evaluated in studies involving simulated and real data. In both experiments, WECS is compared to other standard approaches. Its performance is shown to be superior to other methods in both real and simulated data. Its use may be extended to small areas of change, with no need for algorithm modifications.

This article warrants future research in different directions, such as: adapting the idea of WECS to different types of images (multispectral, polarimetric SAR, etc.); extending energy correlation screening for distinct smoothing techniques; deducing theoretical change detection rates for appropriate statistical models.

Acknowledgment

The authors would like to thank the European Space Agency (ESA) for providing the Sentinel-1 data used in this research. The methods CVA, PCAKM, IRMAD, and ISFA were applied using the codes available at the repository https://github.

com/ChenHongruixuan/ChangeDetectionRepository. The authors would also like to thank the anonymous referees and the editors for their comments, which greatly improved the article's results and presentation.

REFERENCES

[1] T. L. Barreto, R. A. Rosa, C. Wimmer, J. B. Nogueira, J. Almeida, and F. A. M. Cappabianco, "Deforestation change detection using high-resolution multi-temporal X-band SAR images and supervised learning classification," in *Proc. IEEE Int. Geosci. Remote Sens. Symp.*, 2016, pp. 5201–5204.

[2] Y. Ban and O. A. Yousif, "Multitemporal spaceborne SAR data for urban change detection in China," *IEEE J. Sel. Topics Appl. Earth Observ. Remote Sens.*, vol. 5, no. 4, pp. 1087–1094, Aug. 2012.

[3] C. Scher, N. C. Steiner, and K. C. McDonald, "Mapping seasonal glacier melt across the Hindu Kush Himalaya with time series synthetic aperture radar (SAR)," *Cryosphere*, vol. 15, no. 9, pp. 4465–4482, 2021.

[4] F. Bovolo and L. Bruzzone, "A detail-preserving scale-driven approach to change detection in multitemporal SAR images," *IEEE Trans. Geosci. Remote Sens.*, vol. 43, no. 12, pp. 2963–2972, Dec. 2005 .

[5] V. Bhateja, A. Tripathi, and A. Gupta, "An improved local statistics filter for denoising of SAR images," in *Recent Advances in Intelligent Informatics. Advances in Intelligent Systems and Computing*, S. M. Thampi, A. Abraham, S. Pal, and J. Rodriguez, Eds. Berlin, Germany: Springer, 2014, vol. 235, pp. 23–25.

[6] X. Ma, H. Shen, L. Zhang, J. Yang, and H. Zhang, "Adaptive anisotropic diffusion method for polarimetric SAR speckle filtering," *IEEE J. Sel. Topics Appl. Earth Observ. Remote Sens.*, vol. 8, no. 3, pp. 1041–1050, Mar. 2015.

[7] P. A. A. Penna and N. D. A. Mascarenhas, "(Non-) homomorphic approaches to denoise intensity SAR images with non-local means and stochastic distances," *Comput. Geosci.*, vol. 111, pp. 127–138, 2018.

[8] Y. Yuan, Y. Wu, Y. Fu, Y. Wu, L. Zhang, and Y. Jiang, "An advanced SAR image despeckling method by Bernoulli-sampling-based self-supervised deep learning," *Remote Sens.*, vol. 13, 2021, Art. no. 3636.

[9] A. Sebastianelli, M. P. D. Rosso, S. L. Ullo, and P. Gamba, "A speckle filter for Sentinel-1 SAR ground range detected data based on residual convolutional neural networks," *IEEE J. Sel. Topics Appl. Earth Observ. Remote Sens.*, vol. 15, pp. 5086–5101, Jun. 20, 2022, doi: 10.1109/JSTARS.2022.3184355.

[10] S. Fukuda and H. Hirosawa, "Suppression of speckle in synthetic aperture radar images using wavelet," *Int. J. Remote Sens.*, vol. 19, no. 3, pp. 507–519, 1998.

[11] Y. Dong, B. C. Forster, A. K. Milne, and G. A. Morgan, "Speckle suppression using recursive wavelet transforms," *Int. J. Remote Sens.*, vol. 19, no. 2, pp. 317–330, 1998.

[12] S. Solbø and T. Eltoft, "λ-WMAP: A statistical speckle filter operating in the wavelet domain," *Int. J. Remote Sens.*, vol. 25, no. 5, pp. 1019–1036, 2004.

[13] A. Vidal-Pantaleoni and D. Martí, "Comparison of different speckle-reduction techniques in SAR images using wavelet transform," *Int. J. Remote Sens.*, vol. 25, no. 22, pp. 4915–4932, 2004.

[14] K. K. Gupta and R. Gupta, "Despeckle and geographical feature extraction in SAR images by wavelet transform," *ISPRS J. Photogrammetry Remote Sens.*, vol. 62, no. 6, pp. 473–484, 2007.

[15] S. Liu, Q. Hu, P. Li, J. Zhao, M. Liu, and Z. Zhu, "Speckle suppression based on weighted nuclear norm minimization and grey theory," *IEEE Trans. Geosci. Remote Sens.*, vol. 57, no. 5, pp. 2700–2708, May 2019.

[16] P. A. A. Penna and N. D. A. Mascarenhas, "SAR speckle nonlocal filtering with statistical modeling of haar wavelet coefficients and stochastic distances," *IEEE Trans. Geosci. Remote Sens.*, vol. 57, no. 9, pp. 7194–7208, Sep. 2019.

[17] R. D. Johnson and E. S. Kasischke, "Change vector analysis: A technique for the multispectral monitoring of land cover and condition," *Int. J. Remote Sens.*, vol. 19, no. 3, pp. 411–426, 1998.

[18] F. Bujor, E. Trouve, L. Valet, J.-M. Nicolas, and J.-P. Rudant, "Application of log-cumulants to the detection of spatiotemporal discontinuities in multitemporal SAR images," *IEEE Trans. Geosci. Remote Sens.*, vol. 42, no. 10, pp. 2073–2084, Oct. 2004.

[19] P. Gamba, F. Dell'Acqua, and G. Lisini, "Change detection of multitemporal SAR data in urban areas combining feature-based and pixel-based techniques," *IEEE Trans. Geosci. Remote Sens.*, vol. 44, no. 10, pp. 2820–2827, Oct. 2006.

[20] T. Celik, "Unsupervised change detection in satellite images using principal component analysis and k-means clustering," *IEEE Geosci. Remote Sens. Lett.*, vol. 6, no. 4, pp. 772–776, Oct. 2009.

[21] W. Zhang, L. Jiao, F. Liu, S. Yang, W. Song, and J. Liu, "Sparse feature clustering network for unsupervised SAR image change detection," *IEEE Trans. Geosci. Remote Sens.*, vol. 60, pp. 1–13, Apr. 18, 2022, Art. no. 5226713, doi: 10.1109/TGRS.2022.3167745.

[22] P. Mastro, G. Masiello, C. Serio, and A. Pepe, "Change detection techniques with synthetic aperture radar images: Experiments with random forests and Sentinel-1 observations," *Remote Sens.*, vol. 14, no. 14, 2022, Art. no. 3323.

[23] K. Zhang, X. Lv, H. Chai, and J. Yao, "Unsupervised SAR image change detection for few changed area based on histogram fitting error minimization," *IEEE Trans. Geosci. Remote Sens.*, vol. 60, pp. 1–19, Jul. 14, 2022, Art. no. 5231819, doi: 10.1109/TGRS.2022.3190977.

[24] W. Zhang, L. Jiao, F. Liu, S. Yang, and J. Liu, "Adaptive contourlet fusion clustering for SAR image change detection," *IEEE Trans. Image Process.*, vol. 31, pp. 2295–2308, Mar. 4, 2022, doi: 10.1109/JSTARS.2022.3166234.

[25] A. A. Nielsen, "The regularized iteratively reweighted MAD method for change detection in multi- and hyperspectral data," *IEEE Trans. Image Process.*, vol. 16, no. 2, pp. 463–478, Feb. 2007.

[26] W. Li, X. Xiao, P. Xiao, H. Wang, and F. Xu, "Change detection in multitemporal SAR images based on slow feature analysis combined with improving image fusion strategy," *IEEE J. Sel. Topics Appl. Earth Observ. Remote Sens.*, vol. 15, pp. 3008–3023, Apr. 11, 2022, doi: 10.1109/JSTARS.2022.3166234.

[27] H. Zhuang, H. Fan, K. Deng, K. Zhang, X. Wang, and M. Wang, "Change detection in SAR images based on progressive nonlocal theory," *IEEE Trans. Geosci. Remote Sens.*, vol. 60, pp. 1–13, Jun. 9, 2022, Art no. 5229213, doi: 10.1109/TGRS.2022.3181583.

[28] X. Zhang et al., "Two-phase object-based deep learning for multi-temporal SAR image change detection," *Remote Sens.*, vol. 12, 2020, Art. no. 548.

[29] R. Wang, J. Zhang, J. Chen, L. Jiao, and M. Wang, "Imbalanced learning-based automatic SAR images change detection by morphologically supervised PCA-Net," *IEEE Geosci. Remote Sens. Lett.*, vol. 16, no. 4, pp. 554–558, Apr. 2019.

[30] J. Liu, M. Gong, J. Zhao, H. Li, and L. Jiao, "Difference representation learning using stacked restricted Boltzmann machines for change detection in SAR images," *Soft Comput.*, vol. 20, pp. 4645–4657, 2016.

[31] H. Chen, L. Jiao, M. Liang, F. Liu, S. Yang, and B. Hou, "Fast unsupervised deep fusion network for change detection of multitemporal SAR images," *Neurocomputing*, vol. 332, pp. 56–70, 2019.

[32] X. Li, Z. Du, Y. Huang, and Z. Tan, "A deep translation (GAN) based change detection network for optical and SAR remote sensing images," *ISPRS J. Photogrammetry Remote Sens.*, vol. 179, pp. 14–34, 2021.

[33] T. T. Lê, A. M. Atto, E. Trouvé, and J.-M. Nicolas, "Adaptive multitemporal SAR image filtering based on the change detection matrix," *IEEE Geosci. Remote Sens. Lett.*, vol. 11, no. 10, pp. 1826–1830, Oct. 2014.

[34] A. M. Atto, E. Trouvé, Y. Berthoumieu, and G. Mercier, "Multidate divergence matrices for the analysis of SAR image time series," *IEEE Trans. Geosci. Remote Sens.*, vol. 51, no. 4, pp. 1922–1938, Apr. 2013.

[35] B. Aiazzi, L. Alparone, S. Baronti, A. Garzelli, and C. Zoppetti, "Nonparametric change detection in multitemporal SAR images based on mean-shift clustering," *IEEE Trans. Geosci. Remote Sens.*, vol. 51, no. 4, pp. 2022–2031, Apr. 2013.

[36] H.-C. Li, T. Celik, N. Longbotham, and W. J. Emery, "Gabor feature based unsupervised change detection of multitemporal SAR images based on two-level clustering," *IEEE Geosci. Remote Sens. Lett.*, vol. 12, no. 12, pp. 2458–2462, Dec. 2015.

[37] M. Jia and L. Wang, "Novel class-relativity non-local means with principal component analysis for multitemporal SAR image change detection," *Int. J. Remote Sens.*, vol. 39, no. 4, pp. 1068–1091, 2018.

[38] A. Pepe, "Use of multi-temporal SAR non-local mean filtering operations for change detection analyses," in *Proc. IEEE 21st Mediterranean Electrotechnical Conf.*, 2022, pp. 616–620.

[39] B. Hou, Q. Wei, Y. Zheng, and S. Wang, "Unsupervised change detection in SAR image based on gauss-log ratio image fusion and compressed projection," *IEEE J. Sel. Topics Appl. Earth Observ. Remote Sens.*, vol. 7, no. 8, pp. 3297–3317, Aug. 2014.

[40] C. Wu, B. Du, and L. Zhang, "Slow feature analysis for change detection in multispectral imagery," *IEEE Trans. Geosci. Remote Sens.*, vol. 52, no. 5, pp. 2858–2874, May 2014.

[41] B. Du, L. Ru, C. Wu, and L. Zhang, "Unsupervised deep slow feature analysis for change detection in multi-temporal remote sensing images," *IEEE Trans. Geosci. Remote Sens.*, vol. 57, no. 12, pp. 9976–9992, Dec. 2019.
[42] Y. Chen, Z. Ming, and M. Menenti, "Change detection algorithm for multitemporal remote sensing images based on adaptive parameter estimation," *IEEE Access*, vol. 8, pp. 106083–106096, 2020.
[43] Y. Lin, Y.-C. Chen, Y.-T. Kuo, and W.-A. Chao, "Performance study of landslide detection using multi-temporal SAR images," *Remote Sens.*, vol. 14, 2022, Art. no. 2444.
[44] H. Hu and Y. Ban, "Unsupervised change detection in multitemporal SAR images over large urban areas," *IEEE J. Sel. Topics Appl. Earth Observ. Remote Sens.*, vol. 7, no. 8, pp. 3248–3261, Aug. 2014.
[45] O. Yousif and Y. Ban, "Improving urban change detection from multitemporal SAR images using PCA-NLM," *IEEE Trans. Geosci. Remote Sens.*, vol. 51, no. 4, pp. 2032–2041, Apr. 2013.
[46] F. Bovolo and L. Bruzzone, "The time variable in data fusion: A change detection perspective," *IEEE Geosci. Remote Sens. Mag.*, vol. 3, no. 3, pp. 8–26, Sep. 2015.
[47] S. Liu, D. Marinelli, L. Bruzzone, and F. Bovolo, "A review of change detection in multitemporal hyperspectral images: Current techniques, applications, and challenges," *IEEE Geosci. Remote Sens. Mag.*, vol. 7, no. 2, pp. 140–158, Jun. 2019.
[48] T. Matsunaga et al., "Current status of hyperspectral imager suite (HISUI) onboard international space station (ISS)," in *Proc. IEEE Int. Geosci. Remote Sens. Symp.*, 2017, pp. 443–446.
[49] L. Bruzzone and D. F. Prieto, "Automatic analysis of the difference image for unsupervised change detection," *IEEE Trans. Geosci. Remote Sens.*, vol. 38, no. 3, pp. 1171–1182, May 2000.
[50] T. Celik, "Change detection in satellite images using a genetic algorithm approach," *IEEE Geosci. Remote Sens. Lett.*, vol. 7, no. 2, pp. 386–390, Apr. 2010.
[51] G. Quin, B. Pinel-Puyssegur, J.-M. Nicolas, and P. Loreaux, "MIMOSA: An automatic change detection method for SAR time series," *IEEE Trans. Geosci. Remote Sens.*, vol. 52, no. 9, pp. 5349–5363, Sep. 2014.
[52] S. Saha, F. Bovolo, and L. Bruzzone, "Change detection in image time-series using unsupervised LSTM," *IEEE Geosci. Remote Sens. Lett.*, vol. 19, pp. 1–5, Dec. 24, 2022, Art no. 8005205, doi: 10.1109/LGRS.2020.3043822.
[53] R. G. Negri et al., "Spectral–spatial-aware unsupervised change detection with stochastic distances and support vector machines," *IEEE Trans. Geosci. Remote Sens.*, vol. 59, no. 4, pp. 2863–2876, Apr. 2021.
[54] R. G. Negri and A. C. Frery, "Unsupervised change detection driven by floating references: A pattern analysis approach," *Pattern Anal. Appl.*, vol. 24, pp. 933–949, 2021.
[55] P. A. Morettin, A. Pinheiro, and B. Vidakovic, *Wavelets in Functional Data Analysis*. Berlin, Germany: Springer, 2017.
[56] J. Fan, R. Li, C.-H. Zhang, and H. Zou, *Statistical Foundations of Data Science*. Boca Raton, FL, USA: CRC Press, 2020.
[57] B. Vidakovic, *Statistical Modeling by Wavelets*. Hoboken, NJ, USA: Wiley, 1999.
[58] R. R. Coifman and D. L. Donoho, "Translation-invariant De-noising," in *Wavelets and Statistics*, A. Antoniadis and G. Oppenheim, Eds. New York, NY, USA: Springer, 1995, pp. 125–150.
[59] J. Fan and J. Lv, "Sure independence screening for ultrahigh dimensional feature space," *J. Roy. Statist. Soc., B*, vol. 70, no. 5, pp. 849–911, 2008.
[60] L. Jia, M. Li, P. Zhang, Y. Wu, L. An, and W. Song, "Remote-sensing image change detection with fusion of multiple wavelet kernels," *IEEE J. Sel. Topics Appl. Earth Observ. Remote Sens.*, vol. 9, no. 8, pp. 3405–3418, Aug. 2016.
[61] T. Celik and K.-K. Ma, "Unsupervised change detection for satellite images using dual-tree complex wavelet transform," *IEEE Trans. Geosci. Remote Sens.*, vol. 48, no. 3, pp. 1199–1210, Mar. 2010.
[62] L. Shu, G. Zhou, D. Liu, J. Huang, R. Zhang, and F. Wang, "On-board wavelet based change detection implementation of SAR flood image," in *Proc. IEEE Int. Geosci. Remote Sens. Symp.*, 2019, pp. 1502–1505.
[63] G. Beylkin, R. Coifman, and V. Rokhlin, "Fast wavelet transforms and numerical algorithms I," *Commun. Pure Appl. Math.*, vol. 44, no. 2, pp. 141–183, 1991.
[64] I. Daubechies, *Ten Lectures on Wavelets*. Philadelphia, PA, USA: SIAM, 1992.
[65] C. J. V. Rijsbergen, *Information Retrieval*, 2nd ed. Oxford, U.K.: Butterworth-Heinemann, 1979.
[66] R. G. Congalton and K. Green, *Assessing the Accuracy of Remotely Sensed Data: Principles and Practices*, 3rd ed. Boca Raton, FL, USA: CRC Press, 2019.
[67] European space agency, "European space agency–Sentinel-1 SAR Technical Guide," 2021 [Online]. Available: https://sentinel.esa.int/web/sentinel/technical-guides/sentinel-1-sar Accessed: Sep. 1, 2021.
[68] N. Otsu, "A threshold selection method from gray-level histograms," *IEEE Trans. Syst., Man, Cybern.*, vol. 9, no. 1, pp. 62–66, Jan. 1979.
[69] J. Kittler and J. Illingworth, "Minimum error thresholding," *Pattern Recognit.*, vol. 19, no. 1, pp. 41–47, 1986.

Rodney V. Fonseca was born in Brazil in 1993. He received a B.Sc. degree in statistics from the Federal University of Ceará, Fortaleza, Brazil, in 2014, an M.Sc. degree in statistics from the Federal University of Pernambuco, Recife, in 2017, and a Ph.D. degree in statistics from Campinas State University, Campinas, Brazil, in 2021.

He is currently a Postdoctoral Fellow with the Department of Computer Science and Applied Mathematics, Weizmann Institute of Science, Rehovot, Israel. His research interests include high-dimensional statistics, time series, and regression models.

Rogério G. Negri received the undergraduate degree in mathematics from Universidade Estadual Paulista (UNESP), São José dos Campos, Brazil, in 2006, and the M.Sc. and Ph.D. degrees in applied computation from Intituto Nacional de Pesquisas Espaciais, São José dos Campos, in 2009 and 2013, respectively.

He is currently Associate Professor with UNESP. His main research interests include pattern recognition and image processing.

Aluísio Pinheiro received the B.S. degree in statistics from the National School of Statistical Sciences, Rio de Janeiro, Brazil, in 1989, the M.S. degree in statistics from the University of Campinas, Campinas, Brazil, in 1992, and the Ph.D. degree in statistics from the University of North Carolina (UNC) at Chapel Hill, Chapel Hill, NC, USA, in 1997.

After Ph.D., he joined the Department of Statistics, University of Campinas, where he was an Assistant and Associate Professor of statistics. In 2012, he was the P. K. Sen Distinguished Visiting Professor of biostatistics with the UNC Gillings School of Global Public Health. He is currently a Professor of statistics with the University of Campinas, Campinas, Brazil. His research interests include nonparametric statistics, especially on generalized U-statistics and wavelet methodologies with applications in high-dimensional data, genetics, education, and biological sciences.

Dr. Pinheiro was on the Governing Board of the Brazilian Statistical Association on two occasions, as General Secretary (2010–2012) and Treasurer (2018–2020).

Abdourrahmane Mahamane Atto (Senior Member, IEEE) received the master's degree in electrical engineering from the Polytechnic Abomey-Calavi, Cotonou, Benin, in 2002, the master's degree in pure and applied mathematics from the University of Abomey-Calavi, Abomey-Calavi, Benin, in 2002, the master's degree in image and artificial intelligence from TELECOM Bretagne, Brest, France, in 2004, the Ph.D. degree in mathematics and applications jointly from the University of Rennes I, Rennes, France and TELECOM Bretagne, in 2008, and the Habilitation degree for research supervision from the ComUE University Grenoble Alpes, Saint-Martin-d'Hères, France, in 2015 .

He is an Associate Professor with the University Savoie Mont Blanc, Polytech Annecy-Chambéry, Le Bourget-du-Lac, France, and a Researcher with the LISTIC Laboratory of Computer Science, Systems, Information and Knowledge Processing, Annecy le Vieux Cedex. His research interests include mathematical methods and models for artificial intelligence, information processing, and image time-series analysis.